



RESEARCH LETTER

10.1002/2016GL069931

Key Points:

- The 2016 earthquake has little seismic wave directivity for an M_w 7.8 strike-slip faulting event
- Aftershocks, surface waves, and finite fault inversions indicate north-south rupture ≤ 70 km long
- The static stress drop is ~ 20 MPa, a high value similar to other events in the intraplate deformation zone

Supporting Information:

- Supporting Information S1
- Movie S1
- Movie S2

Correspondence to:

T. Lay,
tlay@ucsc.edu

Citation:

Lay, T., L. Ye, C. J. Ammon, A. Dunham, and K. D. Koper (2016), The 2 March 2016 Wharton Basin M_w 7.8 earthquake: High stress drop north-south strike-slip rupture in the diffuse oceanic deformation zone between the Indian and Australian Plates, *Geophys. Res. Lett.*, *43*, 7937–7945, doi:10.1002/2016GL069931.

Received 6 JUN 2016

Accepted 21 JUL 2016

Accepted article online 25 JUL 2016

Published online 4 AUG 2016

The 2 March 2016 Wharton Basin M_w 7.8 earthquake: High stress drop north-south strike-slip rupture in the diffuse oceanic deformation zone between the Indian and Australian Plates

Thorne Lay¹, Lingling Ye², Charles J. Ammon³, Audrey Dunham³, and Keith D. Koper⁴

¹Department of Earth and Planetary Sciences, University of California, Santa Cruz, California, USA, ²Seismological Laboratory, California Institute of Technology, Pasadena, California, USA, ³Department of Geosciences, Pennsylvania State University, University Park, Pennsylvania, USA, ⁴Department of Geology and Geophysics, University of Utah, Salt Lake City, Utah, USA

Abstract The diffuse deformation zone between the Indian and Australian plates has hosted numerous major and great earthquakes during the seismological record, including the 11 April 2012 M_w 8.6 event, the largest recorded intraplate earthquake. On 2 March 2016, an M_w 7.8 strike-slip faulting earthquake occurred in the northwestern Wharton Basin, in a region bracketed by north-south trending fracture zones with no previously recorded large event nearby. Despite the large magnitude, only minor source finiteness is evident in aftershock locations or resolvable from seismic wave processing including high-frequency P wave backprojections and Love wave directivity analysis. Our analyses indicate that the event ruptured bilaterally on a north-south trending fault over a length of up to 70 km, with rupture speed of ≤ 2 km/s, and a total duration of ~ 35 s. The estimated stress drop, ~ 20 MPa, is high, comparable to estimates for other large events in this broad intraplate oceanic deformation zone.

1. Introduction

Seismogenic strain release in the lithosphere below the central Indian Ocean is significant and distributed over a region comparable in size to the conterminous United States (Figure 1). Global plate motion models indicate that internal deformation within the diffuse boundary between the Indian and Australian plates accommodates ~ 11 mm/yr of relative movement [e.g., *Wiens et al.*, 1985; *Gordon et al.*, 1990; *Royer et al.*, 1997; *Delescluse and Chamot-Rooke*, 2007; *Demets et al.*, 2010]. The broad region has hosted numerous major and great earthquakes. The largest ones involve strike-slip faulting, although thrust faulting is observed in the southern and western portions of the region (see Figure S1 in the supporting information). The Australian plate east of the Ninety East Ridge has numerous north-south striking fracture zones associated with left-lateral offsets of the east-west trending Wharton fossil spreading center, which was active between 45 and 85 Ma [e.g., *Deplus et al.*, 1998; *Matthews et al.*, 2011]. Some of these structures appear to influence earthquake faulting geometry or are directly reactivated by present day deformation within the intraplate oceanic basins and in the subducting slab [e.g., *Bull and Scrutton*, 1990; *Deplus et al.*, 1998; *Abercrombie et al.*, 2003; *Delescluse et al.*, 2008; *Rajendran et al.*, 2011; *Geersen et al.*, 2015; *Aderhold and Abercrombie*, 2016].

The combined plate boundary stresses resulting from the Himalayan collision along the northern Indian plate and from slab pull due to subduction of the Australian plate along the Sunda megathrust [e.g., *Delescluse et al.*, 2012] account for the prevalence of strike-slip faulting in the intraplate deformation zone, even close to the trench where outer rise extension is typically observed in other zones. The 11 April 2012 M_w 8.6 and 8.2 great strike-slip earthquakes (Figure 1) ruptured a mix of north-south and east-west trending strike slip faults in the Cocos Basin (north Wharton Basin) [e.g., *Duputel et al.*, 2012; *Satriano et al.*, 2012; *Meng et al.*, 2012; *Yue et al.*, 2012; *Ishii et al.*, 2013; *Wei et al.*, 2013; *Hill et al.*, 2015], and there are many other strike-slip events along the outer rise (Figure S1). The M_w 8.6 earthquake is the largest recorded intraplate event and also the largest recorded strike-slip event. *Hill et al.* [2015] estimate an average stress drop of 17 MPa for this event. The Wharton Basin extends southeast of these events and has experienced other large, predominantly strike-slip earthquakes such as the 18 June 2000 M_w 7.9 earthquake (Figure 1) west of the Investigator Fracture Zone [*Robinson et al.*, 2001; *Abercrombie et al.*, 2003]. This event included secondary faulting on a thrust fault, but the stress drop for the primary strike-slip rupture was estimated as 5–10 MPa by *Abercrombie et al.* [2003] and 20 MPa by *Robinson et al.* [2001].

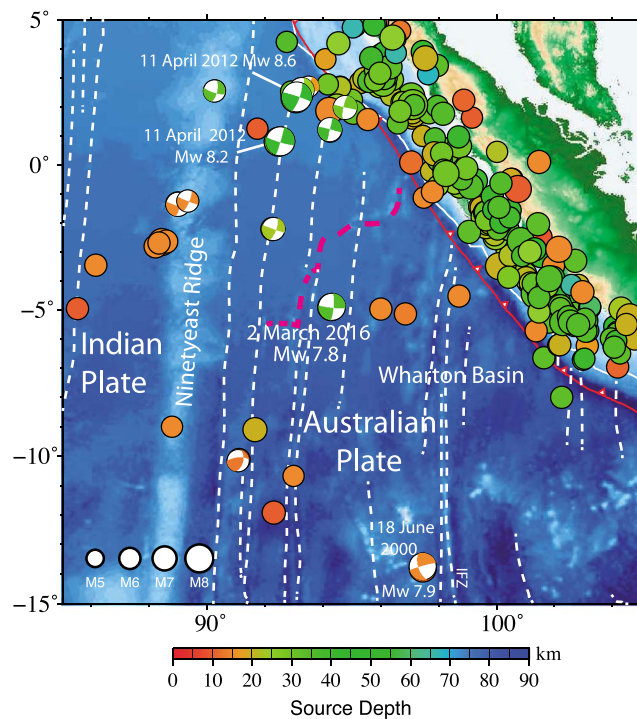


Figure 1. Map of large (magnitude ≥ 6.0) seismicity recorded earthquakes from 1900 to 2016 in the tectonic environment surrounding the 2 March 2016 Wharton Basin M_w 7.8 earthquake. Circles indicate earthquake epicenters from the USGS-NEIC catalog, color-coded for source depth and with radius scaled proportional to magnitude. The best double-couple geometries of the centroid-moment tensor solutions for those events from 1976 to present located in the sub-oceanic Indian and Australian plates from the GCMT catalog are shown at the NEIC location. The largest intraplate ruptures are labeled. White dashed curves are tracks of fracture zones from *Matthews et al.* [2011]. The Investigator Fracture Zone is labeled IFZ. The dashed magenta curve is the fossil Wharton ridge location. Maps with all recorded seismicity and all GCMT focal mechanisms from 1976 to present are shown in Figure S1.

2.1. Long-Period Faulting Mechanism

The long-period point-source moment tensor solutions for the 2 March 2016 event reported by the USGS-NEIC W phase inversion ($M_0 = 5.85 \times 10^{20}$ Nm; strike $\phi_1 = 5^\circ$; dip $\delta_1 = 79^\circ$; rake $\lambda_1 = 6^\circ$; $\phi_2 = 274^\circ$; $\delta_2 = 84^\circ$; and $\lambda = 169^\circ$) and the quick Global Centroid-Moment Tensor (GCMT) project ($M_0 = 5.81 \times 10^{20}$ Nm; strike $\phi_1 = 5^\circ$; dip $\delta_1 = 80^\circ$; rake $\lambda_1 = -6^\circ$; $\phi_2 = 96^\circ$; dip $\delta_2 = 84^\circ$; and rake $\lambda_2 = -170^\circ$) (<http://www.globalcmt.org/CMTsearch.html>) indicate that the primary faulting geometry is strike slip with north-south and east-west trending nodal planes. The centroid time shifts are 18.0 and 15.4 s, and the centroid depths are 40.5 and 34.6 km, respectively, comparable to those reported for the 2012 earthquakes to the north [e.g., *Duputel et al.*, 2012]. We test the stability of the large depth estimates with our own W phase inversions following the procedure of *Kanamori and Rivera* [2008]. We invert low-frequency ground motions in the range 1.7 to 10 mHz using different selection criteria and up to 129 channels, finding similar faulting geometries to those listed above, but preferred centroid depths of 19.5–21.5 km. Thus, we do not attach significance to the original large centroid depth estimates.

2.2. Aftershocks

The epicenters of 20 aftershocks located by the USGS-NEIC are shown in Figure 2. These events range in magnitude from 4.1 to 5.6, and all have depth estimates less than 18 km. Two aftershocks also have quick GCMT solutions, shown in Figure 2; both have strike-slip mechanisms. Locating earthquakes in such a remote

On 2 March 2016 a major, M_w 7.8, intraplate strike-slip earthquake ruptured in the northwestern Wharton Basin, south of the Wharton fossil spreading center, about 600 km southwest from the Sumatra subduction zone (Figure 1). We analyze seismic data to constrain the 2016 event faulting process. Events such as this provide valuable information about the seismogenic deformation process and stress state in the deforming oceanic lithosphere.

2. Rupture Characteristics of the 2016 Event

The United States Geological Survey National Earthquake Information Center (USGS-NEIC) reports a hypocenter for the 2 March 2016 earthquake at 4.952°S , 94.330°E , 24.0 km deep at an origin time of 12:49:48.11 UTC (<http://earthquake.usgs.gov/earthquakes/eventpage/us10004u1y#executive>). No historical seismicity has been located in the source region. The 2016 event is offset from two prominent north-south trending fracture zones to the west (Figures 1 and S1) and zones with more subtle bathymetric expressions to the east; the precise location of faulting does not have a clear bathymetric expression [*Matthews et al.*, 2011].

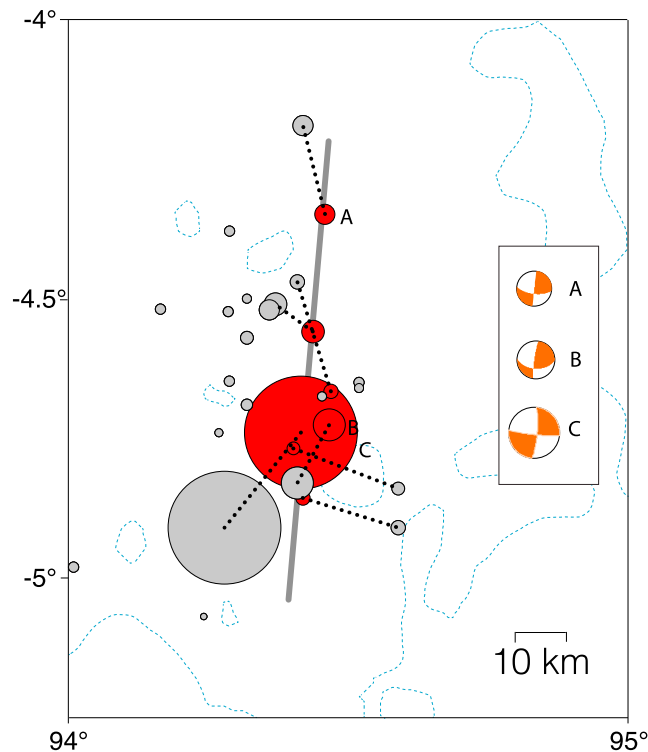


Figure 2. Epicentral locations of all events located by the USGS-NEIC from 2 March 2016 to 22 April 2016 (gray circles with area scaled proportional to seismic moment). The red circles indicate the relocated positions of the main shock and six aftershocks obtained using the double difference surface wave relative location method (with dotted lines indicating the shift relative to the initial NEIC locations). Three rapid GCMT best double-couple focal mechanism solutions are shown for the main shock and two aftershocks. Dotted blue contours indicate mild bathymetric topography.

region is challenging, and although the aftershocks show a general elongation in the north-south direction, tight constraints on the rupture extent are not obvious.

Given the remote location and small sizes of many events, we relocate the larger earthquakes using the relative surface wave relocation procedure of *Cleveland and Ammon* [2013] and *Cleveland et al.* [2015]. The method is based on cross-correlation estimated relative time shifts measured from R1 and G1 phases filtered to the 30 to 80 s period passband. We visually examine each waveform for adequate signal-to-noise characteristics. Double-difference relative time shifts are inverted for the relative centroid latitudes and longitudes (epicentroids) and centroid times of the events using an iteratively reweighted double-difference approach [*Cleveland and Ammon*, 2013]. Initial locations and origin times are from the early NEIC estimates. The main shock and six aftershocks have adequate signal quality to apply this procedure, which results in the relocations shown by red symbols in Figure 2. Events moved from 10 to 20 km, and the mean centroid time shift for the main shock

was about 13 s. The seven events are more tightly clustered after relocation and more clearly define a trend consistent with the nodal planes striking 5° in the *W* phase and GCMT solutions. Epicentroid relative uncertainty estimates are on the order of a few kilometers [*Cleveland and Ammon*, 2013], and the spatial extent of the relocation pattern trades off with surface-wave slowness. We assume R1 and G1 speeds of 4.1 km/s and 4.3 km/s.

2.3. Backprojection Analysis

Backprojection of short-period *P* waves from regional and global networks has proved valuable for identifying fault planes, rupture extent, and rupture speed for many events since the initial application to the 2004 Sumatra earthquake [*Ishii et al.*, 2005; *Krüger and Ohrnberger*, 2005]. We use the method described by *Xu et al.* [2009] to backproject teleseismic *P* wave recordings in the period range 0.5–2.0 s from large aperture networks of 53 stations in Australia and 127 stations in Europe to a horizontal subevent grid centered on the source region. Array response figures for the two networks are shown in Figure S2. The results are most reliable for the European configuration (Figures 3a and 3b) based on the lower level of image streaking, with indication of bilateral rupture along the north-south direction. The results for the Australian network (Figures 3c and 3d) are more affected by limited spatial resolution. The backprojections indicate a concentrated source region, with overall dimension less than ~70 km and total duration less than ~40 s. Backprojection animations are given in Movie S1 in the supporting information.

2.4. Surface-Wave Directivity Analysis

Surface waves are especially sensitive to source finiteness and directivity because they propagate with speeds similar to typical rupture speeds. As a first-order assessment of surface wave directivity, we equalize broadband short-arc Rayleigh and Love wave recordings to a propagation distance of 90° by correcting

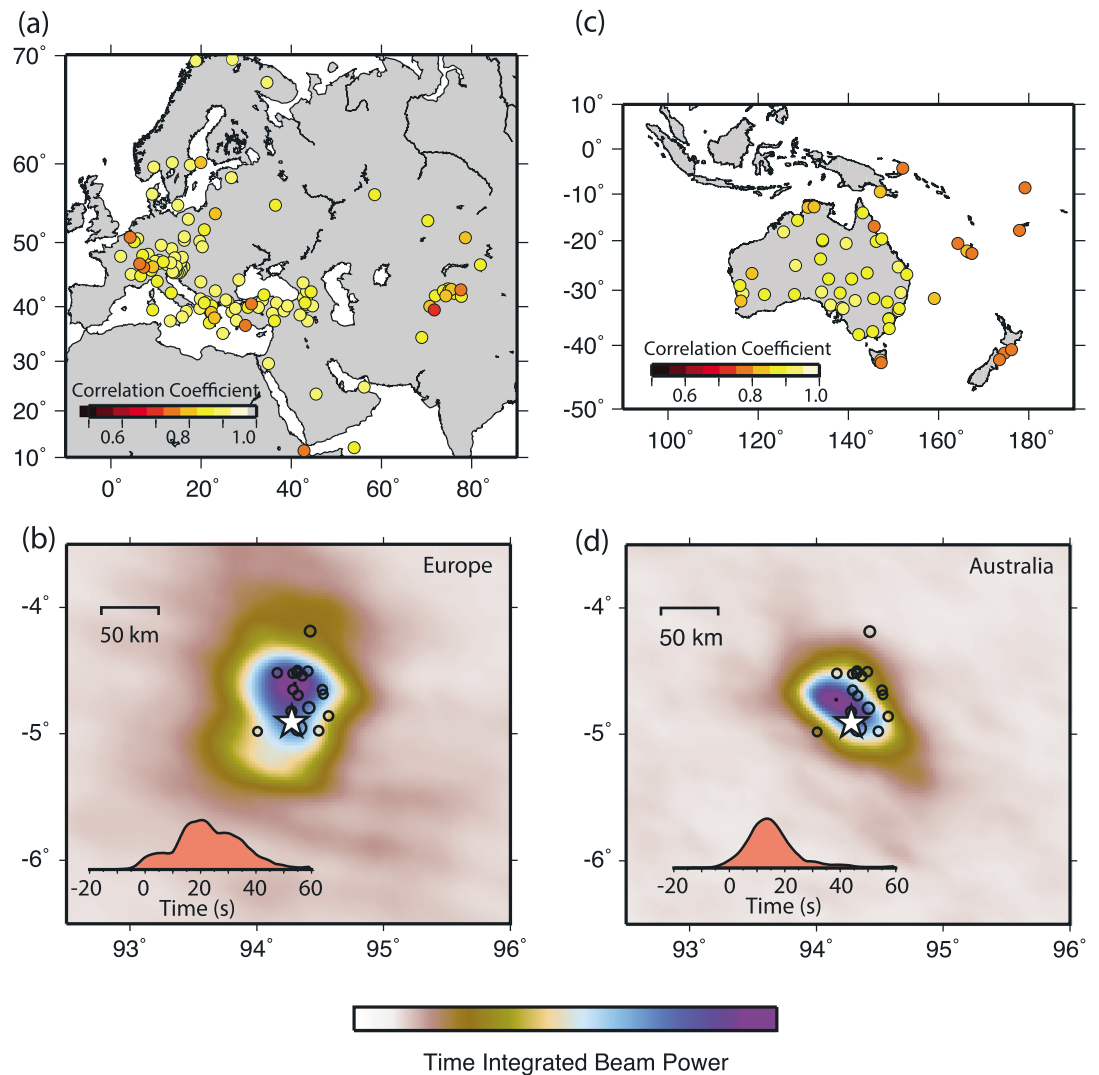


Figure 3. Backprojection analysis using 0.5 to 2.0 s period teleseismic P waves from large aperture networks around (a) Europe and (c) Australia, with the station locations and the relative broadband signal correlation for the early part of the signal being shown. (b and d) Time-integrated power distributions of the backprojection images are shown for Europe and Australia, respectively. The red insets show backprojection fourth root stacked signal power as a function of time, the white star is the main shock epicenter, and the black circles are NEIC epicenters of aftershocks occurring through 10 March 2016. Animations of the backprojections are provided in Movie S1 in the supporting information.

for attenuation and geometric spreading. For ground displacement signals in the period range 50–200 s, the data show clear four-lobed amplitude patterns as expected for a strike-slip event (Figure S3). There is localized enhancement of $R1$ amplitudes at azimuths near 30° and 315° but, otherwise, no systematic variation with respect to the source. This indicates that there is no strong unilateral directivity in the source affecting long periods.

Broadband surface wave source time functions are among the best teleseismic indicators of source finiteness and directivity [e.g., Ammon *et al.*, 2006]. Surface wave observations must be accurately corrected for all propagation effects to determine the source time functions. Given that the 2 March 2016 event appears to have a compact source area, we require short-period signals to resolve any finiteness, so we use empirical Green's functions (EGF) rather than model-based corrections. The M_w 5.7 aftershock on 3 March 2016 (4.80°S , 94.41°E) has similar focal mechanism (USGS-NEIC W phase $M_0 = 2.73 \times 10^{17}$ Nm; $\phi_1 = 2^\circ$, $\delta_1 = 89^\circ$, $\lambda_1 = -12^\circ$; and depth 11.5 km) and relocated epicenter (Figure 2) to the main shock and good quality surface wave recordings, so we use its signals as EGFs. The centroid depth of the EGF event is within the large-slip depth

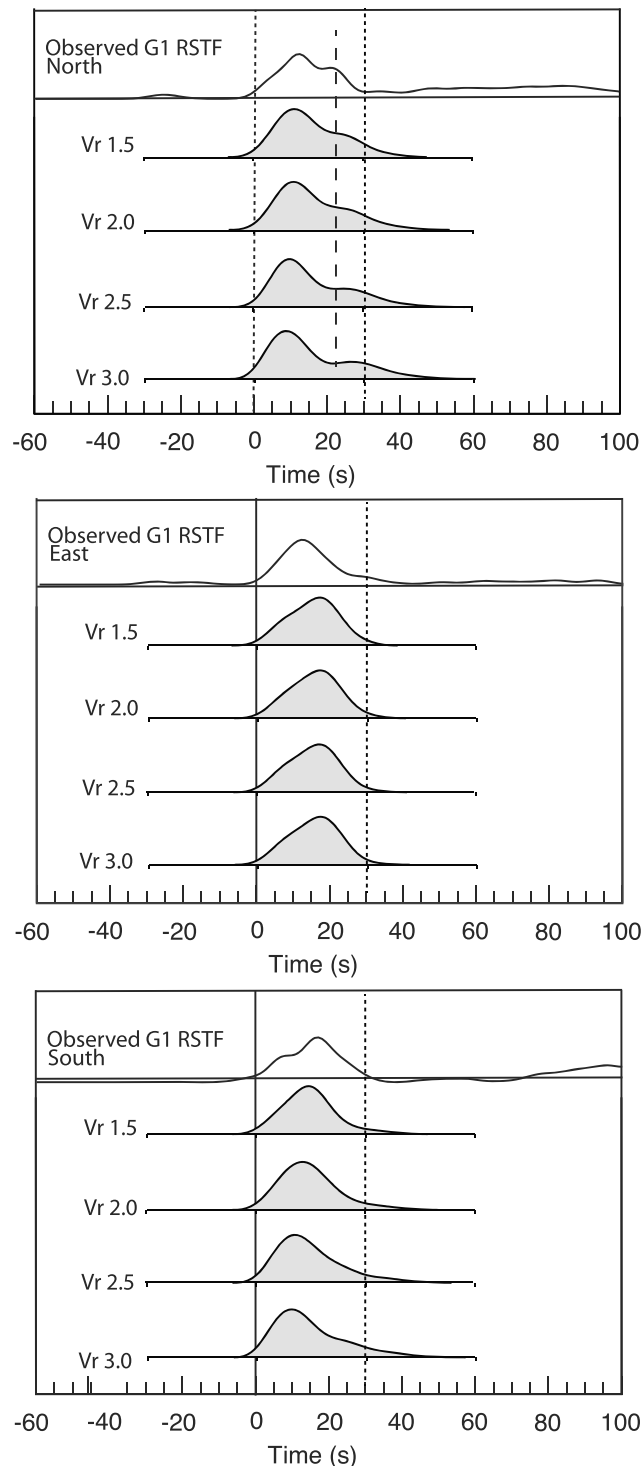


Figure 4. Observed Love wave (G1) relative source time functions (RSTFs) at different azimuths obtained by deconvolving the corresponding EGF signals are compared with predicted source time functions from the finite fault source models that use varying rupture expansion speeds from 1.5 to 3.0 km/s and a strike of 5°. The overall RSTF duration is about 30 s at all azimuths, with variation in the shape of the RSTFs consistent with bilateral rupture on the north-south fault. The observations are best matched by models with rupture speeds of 2 km/s or less, with higher speeds resulting in slightly too large of a total duration to the north and south.

range for the main shock, and we suppress short-period signals to permit the use of an EGF that does not exactly match the centroid depth of the main shock. We visually screened all waveforms to identify signals with suitable signal-to-noise characteristics. We use both an iterative time-domain deconvolution with positivity constraints and a water-level spectral approach to estimate relative source time functions (RSTFs) for short-arc Rayleigh and Love wave signals [e.g., Ammon *et al.*, 2006]. We estimate the main shock duration and directivity characteristics using a group velocity window of 5 km/s to 2.5 km/s.

Surprisingly, for such a large strike-slip event, the RSTFs show little evidence of horizontal rupture directivity, indicating a relatively compact source. The time-domain deconvolved RSTFs for G1 Love waves do not provide strong preference between rupture azimuths of 5° or 95° in terms of systematic variations in duration (Figure S4). However, the north-south alignment has less variable waveforms for stations in different azimuthal ranges. Figure 4 shows representative G1 RSTFs at three azimuths, with the northerly azimuth having a strong first peak and weak second peak while the southerly azimuth has a weak first peak and strong second peak. This is suggestive of asymmetric bilateral rupture, as modeled below. Frequency-domain deconvolutions are noisier, but show no indication of any unusual rupture complexity or secondary faulting [e.g., Lay *et al.*, 2010]. Deconvolution of SH waves using the same EGF event also does not reveal strong directivity patterns for the two rupture directions (Figure S5), and the higher signal phase velocity leads to only slight broadening of the RSTFs to the north and south relative to the east (Figure S6), again, consistent with bilateral slip.

2.5. Finite Fault Modeling

Finite fault slip evolution models for the 2016 event are obtained by inverting 74 P wave ground displacements and 61 SH wave ground velocities in the pass-band 0.005–0.9 Hz. SH signals are given

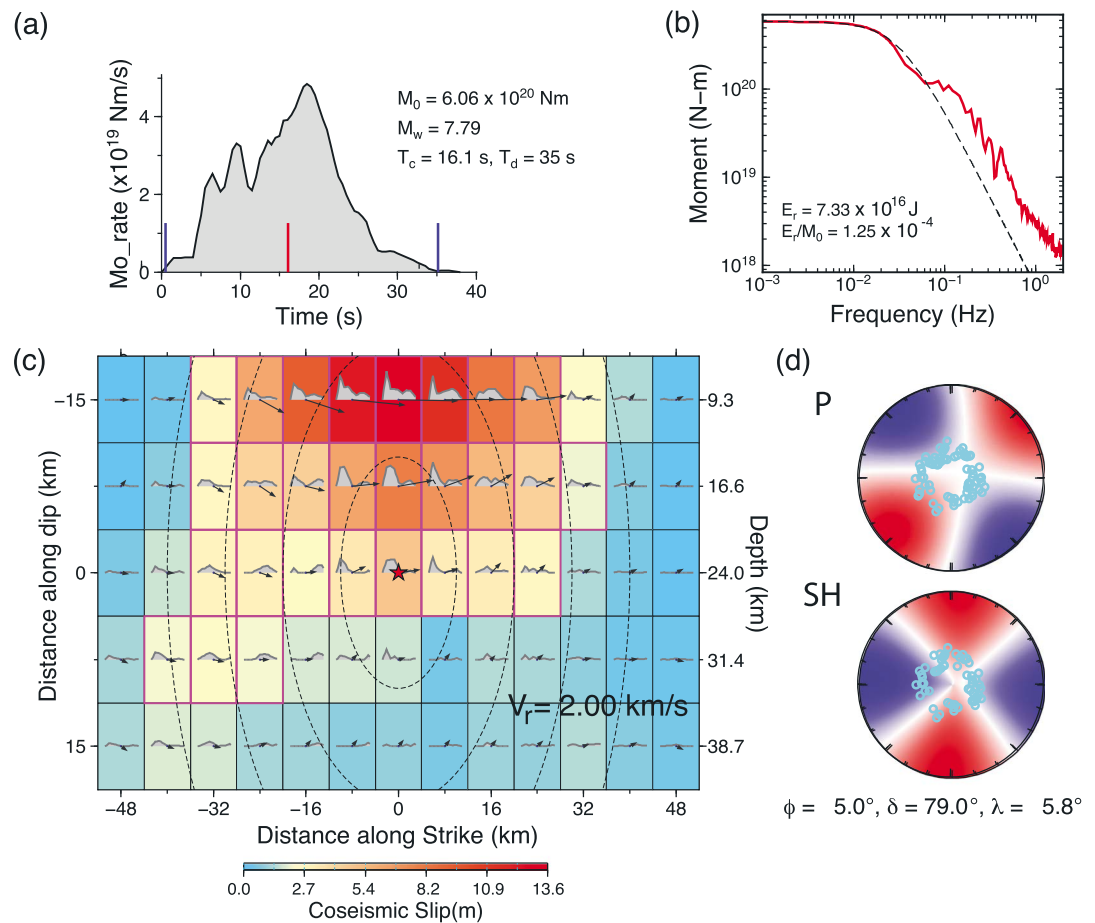


Figure 5. The preferred source model for the 2 March 2016 M_w 7.8 Wharton Basin earthquake. The fault model has a strike, $\phi = 5^\circ$, dip $\delta = 79^\circ$ and average rake $\lambda = 5.8^\circ$, with a rupture speed of 2.0 km/s. (a) The moment rate function for the finite fault slip distribution, with seismic moment M_0 , M_w , centroid time T_c , and total duration T_d being shown. (b) Far-field source spectrum for the event, with the spectrum of the moment rate function in Figure 5a used for frequencies less than 0.05 Hz and logarithmically averaged P wave displacement spectra corrected for radiation pattern, geometric spreading, and attenuation used for frequencies from 0.05 to 2.0 Hz. A reference ω -squared spectrum with the same moment and a stress parameter of 3 MPa is shown in the dashed line. The broadband radiated energy E_r and moment-scaled radiated energy E_r/M_0 are shown. (c) Finite-fault slip distribution with slip color coded and indicated by the vectors in each subfault, along with the subfault source time functions. Dashed lines indicate 5 s rupture isochrones. (d) P and SH radiation patterns and lower hemisphere data sampling for waveforms used in the inversion and the average focal mechanism. Animation of the slip history is presented in Movie S2 in the supporting information.

weights of 0.5 relative to P waves. We use a least squares kinematic inversion method [Hartzell and Heaton, 1983; Kikuchi and Kanamori, 1991] with a positivity constraint, constant rupture expansion speed (V_r), specified fault geometry, variable subfault rake, and subfault source time functions parameterized by eight overlapping 1.5 s rise-time triangles (for the final model). The fault grid has five rows with 7.5 km subfault widths along dip and 13 columns along strike with lengths given by 4 times the rupture speed (8 km for 2.0 km/s). Models are computed for a wide range of rupture speeds with bilateral grids along nodal planes of the W phase and GCMT solutions. The slightly northward dipping east-west fault plane of the W phase solution fits waveform better than the slightly southward dip of the corresponding plane of the GCMT solution, with both cases indicating some eastward directivity over 10–20 km, similar to that found by the USGS-NEIC. The north-south plane from both long-period solutions gives mostly similar waveform fits but with $\sim 3\%$ higher residual waveform power than for the east-west plane. Based on the combined indications of north-south faulting inferred from aftershocks and surface wave RSTFs, we prefer the solutions with a strike of 5° .

For the north-south fault model cases, inversions with different rupture speeds produce predicted surface wave source functions in better agreement with the G1 observations for $V_r \leq 2.0$ km/s (Figure 4), as higher

speeds tend to slightly over estimate the total duration and the separation of the two pulses toward the north. Lower speeds match the azimuthal variation in peak source function arrival time better. The bilateral slip model for $V_r = 2.0$ km/s is shown in Figure 5, with the moment rate function having a total duration of 35 s, a centroid time of 16.1 s, and $M_0 = 6.06 \times 10^{20}$ Nm (M_w 7.8). There is slight northward asymmetry in the rupture, although not as much as found in the USGS-NEIC finite fault for this nodal plane. Peak slip is not well resolved but exceeds 10 m in the shallowest row of the model, and the centroid depth of the slip distribution is 18 km, which is reasonably consistent with our W phase estimates of 19.5–21.5 km. The observed and predicted waveforms for this model are shown in Figure S7; the model accounts for about 79% of the signal power.

2.6. Radiated Seismic Energy and Stress Drop

We calculate the azimuthally averaged far-field source spectra and seismic moment-scaled radiated energy (E_R/M_0) for the 2016 event. The broadband source spectrum (Figure 5b) is obtained by combining the spectrum of the moment-rate function for the finite fault model in Figure 5c for frequencies less than ~ 0.05 Hz with averaged P wave spectra for frequencies from 0.05 to 2.0 Hz. The source spectrum is enriched in short-period source strength above 0.1 Hz relative to the reference spectrum. Average radiated energy from individual P wave spectra is estimated following the procedure of Venkataraman and Kanamori [2004], and the added contribution from lower frequencies is accounted for as described by Ye *et al.* [2016]. More than 94% of the energy is from frequencies > 0.05 Hz. The radiated energy $E_R = 7.3 \times 10^{16}$ J for frequencies up to 1 Hz. There is at least a factor of two uncertainties in radiated energy estimates for a fixed passband due to differing assumptions made among existing procedures. The seismic moment-scaled radiated energy (E_R/M_0) is $\sim 1.25 \times 10^{-4}$, using the finite fault $M_0 = 6.06 \times 10^{20}$ Nm. The ratio is high relative to typical values, which are less than 3×10^{-5} for interplate thrust earthquakes [e.g., Ye *et al.*, 2016] and even higher than found for other large strike slip events.

The static stress drop for the main shock is calculated from the slip model in Figure 5 following two procedures discussed in Ye *et al.* [2016]. The first estimate is obtained by eliminating subfaults with seismic moment less than 15% of the peak subfault seismic moment and then using the remaining average slip and slip area in a circular uniform slip calculation; this gives $\Delta\sigma_{0.15} = 15$ MPa. The second method calculates the shear stress at each subfault produced by the entire dislocation field (Figure S8) and computes a slip weighted average stress drop, $\Delta\sigma_E = 20$ MPa. These estimates increase for lower assumed rupture speed, with values around 26 MPa being found for $V_r = 1.5$ km/s.

3. Discussion and Conclusions

The 2 March 2016 Wharton Basin earthquake has limited spatial extent for an M_w 7.8 strike-slip rupture, with the total bilateral length being estimated as less than 70 km. This rupture length is in stark contrast to that of, for example, the 200+ km long rupture of the 17 November 2013 M_w 7.8 Scotia Ridge earthquake [Ye *et al.*, 2014] located on an active oceanic transform fault or the 300–470 km long rupture of the 1906 San Francisco M 7.7–7.9 earthquake [Wald *et al.*, 1993; Thatcher *et al.*, 1997]. The compact dimension and shallow concentration of slip for the 2016 event result in a high stress drop estimate of 15 to 20 MPa, comparable to estimates for the 11 April 2012 and 18 June 2000 large strike slip events within the broad Wharton Basin intraplate deformation zone and higher than typical values for other large strike slip events [e.g., Ye *et al.*, 2014]. The source duration is less than 35 s, and the modeled rupture speed is less than 2 km/s, but the lack of directivity effects makes details of the rupture hard to resolve. The radiated energy is quite high, but the number of aftershocks is modest for this size event.

The preferred north-south fault orientation is similar to the orientation of nearby fracture zones, but the event does not locate directly on a prominent structure. The fossil spreading ridge to the north trends east-west (Figure 1), so the rupture transects ridge parallel fabric. Possibly, there could be a minor fracture zone feature with little bathymetric expression along the rupture, or the rupture is influenced by the adjacent fracture zone orientations such that it cuts through ridge-parallel features. The isolated position of this rupture and lack of nearby seismicity are akin to prior large events in the deformation zone; low strain rates and relatively strong faults are likely responsible.

The stress orientation implied by the faulting geometry is consistent with other earthquakes in the region east of the Ninety East ridge [e.g., Aderhold and Abercrombie, 2016] and expected from numerical models

of the strain induced by plate collision and subduction on the northern margin of the Indo-Australian plate [e.g., Coblenz *et al.*, 1998]. The routine long-period moment tensor centroid depth estimates are quite deep, similar to the values of the large 2012 events to the north. The oceanic lithosphere in the region of the 2016 earthquake is roughly 40–50 Ma so that assuming a simple plate cooling model places an estimate of the 600° isotherm in the region near a depth of ~35 km. Our modeling suggests that the deep centroid estimates from routine long-period modeling using preliminary reference Earth model (PREM) may have overestimated the true depth of the event and that the main slip is clearly confined to be above the 600° isotherm.

The 2016 event illustrates the importance of detailed analysis of large intraplate ruptures, as they exhibit distinct rupture processes that may not be revealed by routine analyses. In this case, the constraint of having only teleseismic data limits the resolution of source characteristics, but bounds on the unusual source process are obtained by combining various seismic analysis procedures.

Acknowledgments

This work made use of GMT and SAC software. We thank M. Cleveland for his help with and use of his relocation software for the aftershock analysis. Gavin Hayes and an anonymous reviewer provided constructive comments on the manuscript. The IRIS DMS data center was used to access the seismic data from Global seismic network and Federation of Digital Seismic Network stations. This work was supported by NSF grant EAR0635570 (T.L.).

References

- Abercrombie, R. E., M. Antolik, and G. Ekström (2003), The June 2000 M_w 7.9 earthquakes south of Sumatra: Deformation in the India-Australia Plate, *J. Geophys. Res.*, *108*(B1), 2018, doi:10.1029/2001JB000674.
- Aderhold, K., and R. E. Abercrombie (2016), Seismotectonics of a diffuse plate boundary: Observations off the Sumatra-Andaman trench, *J. Geophys. Res. Solid Earth*, *121*, 3462–3478, doi:10.1002/2015JB012721.
- Ammon, C. J., A. A. Velasco, and T. Lay (2006), Rapid determination of first-order rupture characteristics for large earthquakes using surface waves: The 2004 Sumatra-Andaman earthquake, *Geophys. Res. Lett.*, *33*, L14314, doi:10.1029/2006GL026303.
- Bull, J. M., and R. A. Scrutton (1990), Fault reactivation in the central Indian Ocean and the rheology of oceanic lithosphere, *Nature*, *344*, 855–858.
- Cleveland, K. M., T. F. VanDeMark, and C. J. Ammon (2015), Precise relative locations for earthquakes in the northeast Pacific region, *J. Geophys. Res. Solid Earth*, *120*, 6960–6976, doi:10.1002/2015JB012161.
- Cleveland, M., and C. J. Ammon (2013), Precise relative earthquake relocation using surface waves, *J. Geophys. Res. Solid Earth*, *118*, 1–12, doi:10.1002/jgrb.50146.
- Coblenz, D. D., S. Zhou, R. R. Hillis, R. M. Richardson, and M. Sandiford (1998), Topography, boundary forces, and the Indo-Australian intraplate stress field, *J. Geophys. Res.*, *103*, 919–931, doi:10.1029/97JB02381.
- Delescluse, M., and N. Chamot-Rooke (2007), Instantaneous deformation and kinematics of the India–Australia Plate, *Geophys. J. Int.*, *168*, 818–842.
- Delescluse, M., L. G. Montési, and N. Chamot-Rooke (2008), Fault reactivation and selective abandonment in the oceanic lithosphere, *Geophys. Res. Lett.*, *35*, L16312, doi:10.1029/2008GL035066.
- Delescluse, M., N. Chamot-Rooke, R. Cattin, L. Fleitout, O. Trubienko, and C. Vigny (2012), April 2012 intra-oceanic seismicity off Sumatra boosted by the Banda-Aceh megathrust, *Nature*, *490*, 240–245, doi:10.1038/nature11520.
- DeMets, C., R. G. Gordon, and D. F. Argus (2010), Geologically current plate motions, *Geophys. J. Int.*, *181*, 1–80, doi:10.1111/j.1365-246X.2009.04491.x.
- Deplus, C., M. Diament, H. Hébert, G. Bertrand, S. Domingues, J. Dubois, J. Malod, P. Patriat, B. Pontoise, and J. J. Sibilla (1998), Direct evidence of active deformation in the eastern Indian oceanic plate, *Geology*, *26*, 131–134.
- Duputel, Z., H. Kanamori, V. C. Tsai, L. Rivera, L. Meng, J.-P. Ampuero, and J. M. Stock (2012), The 2012 Sumatra great earthquake sequence, *Earth Planet. Sci. Lett.*, *351–352*, 247–257, doi:10.1016/j.epsl.2012.07.017.
- Geersen, J., J. M. Bull, L. C. McNeill, T. J. Henstock, C. Gaedicke, N. Chamot-Rooke, and M. Delescluse (2015), Pervasive deformation of an oceanic plate and relationship to large $> M_w$ 8 intraplate earthquakes: The northern Wharton Basin, Indian Ocean, *Geology*, *43*, 359–362.
- Gordon, R. G., C. DeMets, and D. F. Argus (1990), Kinematic constraints on distributed lithospheric deformation in the equatorial Indian Ocean from present motion between the Australian and India plates, *Tectonics*, *9*, 409–422, doi:10.1029/TC009i003p0409.
- Hartzell, S. H., and T. H. Heaton (1983), Inversion of strong ground motion and teleseismic waveform data for the fault rupture history of the 1979 Imperial Valley, California, earthquake, *Bull. Seismol. Soc. Am.*, *73*(6A), 1553–1583.
- Hill, E. M., et al. (2015), The 2012 M_w 8.6 Wharton Basin sequence: A cascade of great earthquakes generated by near-orthogonal, young, oceanic-mantle faults, *J. Geophys. Res. Solid Earth*, *120*, 3723–3747, doi:10.1002/2014JB011703.
- Ishii, M., P. M. Shearer, H. Houston, and J. E. Vidale (2005), Extent, duration and speed of the 2004 Sumatra-Andaman earthquake imaged by the Hi-net array, *Nature*, *435*, 933–936.
- Ishii, M., E. Kiser, and E. L. Geist (2013), M_w 8.6 Sumatran earthquake of 11 April 2012: Rare seaward expression of oblique subduction, *Geology*, *41*, 319–322.
- Kanamori, H., and L. Rivera (2008), Source inversion of W phase: Speeding up seismic tsunami warning, *Geophys. J. Int.*, *175*, 222–238, doi:10.1111/j.1365-246X.2008.03887.x.
- Kikuchi, M., and H. Kanamori (1991), Inversion of complex body waves—III, *Bull. Seismol. Soc. Am.*, *81*(6), 2335–2350.
- Krüger, F., and M. Ohrnberger (2005), Tracking the rupture of the $M_w = 9.3$ Sumatra earthquake over 1,150 km at teleseismic distance, *Nature*, *435*, 937–939, doi:10.1038/nature03696.
- Lay, T., C. J. Ammon, H. Kanamori, L. Rivera, K. D. Koper, and A. R. Hutko (2010), The 2009 Samoa-Tonga great earthquake triggered doublet, *Nature*, *466*, 964–968, doi:10.1038/nature09214.
- Matthews, K. J., R. D. Müller, P. Wessel, and J. M. Whittaker (2011), The tectonic fabric of the ocean basins, *J. Geophys. Res.*, *116*, B12109, doi:10.1029/2011JB008413.
- Meng, L., J.-P. Ampuero, J. Stock, Z. Duputel, Y. Luo, and V. C. Tsai (2012), Earthquake in a maze: Compressional rupture branching during the 2012 M_w 8.6 Sumatra earthquake, *Science*, *337*, 724–726.
- Rajendran, K., V. Andrade, and C. P. Rajendran (2011), The June 2010 Nicobar earthquake: Fault reactivation on the subduction oceanic plate, *Bull. Seismol. Soc. Am.*, *101*, 2568–2577.
- Robinson, D. P., C. Henry, S. Das, and J. H. Woodhouse (2001), Simultaneous rupture along two conjugate planes of the Wharton Basin earthquake, *Science*, *292*, 1145–1148.

- Royer, J.-Y., R. G. Gordon, C. DeMets, and P. R. Vogt (1997), New limits on the motion between India and Australia since Chron 5 (11 Ma) and implications for lithospheric deformation in the equatorial Indian Ocean, *Geophys. J. Int.*, *129*, 41–74.
- Satriano, C., E. Kiraly, P. Bernard, and J.-P. Vilotte (2012), The 2012 M_w 8.6 Sumatra earthquake: Evidence of westward sequential seismic ruptures associated to the reactivation of a N-S ocean fabric, *Geophys. Res. Lett.*, *39*, L15302, doi:10.1029/2012GL052387.
- Thatcher, W., G. Marshall, and M. Lisowski (1997), Resolution of fault slip along the 470-km-long rupture of the great 1906 San Francisco earthquake and its implications, *J. Geophys. Res.*, *102*, 5353–5367, doi:10.1029/96JB03486.
- Venkataraman, A., and H. Kanamori (2004), Effect of directivity on estimates of radiated seismic energy, *J. Geophys. Res.*, *109*, B04301, doi:10.1029/2003JB002548.
- Wald, D. J., H. Kanamori, D. V. Helmlinger, and T. H. Heaton (1993), Source study of the 1906 San Francisco earthquake, *Bull. Seismol. Soc. Am.*, *83*, 981–1019.
- Wei, S., D. Helmlinger, and J.-P. Avouac (2013), Modeling the 2012 Wharton basin earthquakes off-Sumatra: Complete lithospheric failure, *J. Geophys. Res. Solid Earth*, *118*, 3592–3609, doi:10.1002/jgrb.50267.
- Wiens, D. A., et al. (1985), A diffuse plate boundary model for Indian Ocean tectonics, *Geophys. Res. Lett.*, *12*, 429–432, doi:10.1029/GL012i007p00429.
- Xu, Y., K. D. Koper, O. Sufri, L. Zhu, and A. R. Hutko (2009), Rupture imaging of the M_w 7.9 12 May 2008 Wenchuan earthquake from back projection of teleseismic P waves, *Geochem. Geophys. Geosyst.*, *10*, Q04006, doi:10.1029/2008GC002335.
- Ye, L., T. Lay, K. D. Koper, R. Smalley, L. Rivera, M. G. Bevis, A. F. Zakrajsek, and F. N. Teferle (2014), Complementary slip distributions of the August 4, 2003 M_w 7.6 and November 17, 2013 M_w 7.8 South Scotia Ridge earthquakes, *Earth Planet. Sci. Lett.*, *401*, 215–226.
- Ye, L., T. Lay, H. Kanamori, and L. Rivera (2016), Rupture characteristics of major and great ($M_w \geq 7.0$) megathrust earthquakes from 1990 to 2015: 1. Source parameter scaling relationships, *J. Geophys. Res. Solid Earth*, *121*, 826–844, doi:10.1002/2015JB012426.
- Yue, H., T. Lay, and K. D. Koper (2012), *En échelon* and orthogonal fault ruptures of the 11 April 2012 great intraplate earthquakes, *Nature*, *490*, 245–249, doi:10.1038/nature11492.